Experimental apatite-fluid interaction and partitioning of rare earth elements at 150 and 250 °C

J. CALEB CHAPPELL[1], ALEXANDER P. GYSI[2,3,*], THOMAS MONECKE[1] , AND ZHAOSHAN CHANG[1]

[1]Center for Mineral Resources Science, Department of Geology and Geological Engineering, Colorado School of Mines, Golden, Colorado 80401, USA

[2]Department of Earth and Environmental Science, New Mexico Institute of Mining and Technology, Socorro, New Mexico 87801, USA

[3]New Mexico Bureau of Geology and Mineral Resources, New Mexico Institute of Mining and Technology, Socorro, New Mexico 87801, USA

Revision 1

E-mail: alexander.gysi@nmt.edu

ABSTRACT

Apatite is a common accessory phase in igneous and metamorphic rocks. Its stability in magmatic-hydrothermal and hydrothermal systems is known to be a key control on the mobility of rare earth elements (REE). To better constrain how apatite is altered during fluid-rock interaction at comparably low temperatures, batch-type apatite dissolution experiments were conducted at 150 and 250 °C at saturated water vapor pressure in acidic to mildly acidic (pH of 2–4) aqueous fluids having variable salinities (0, 0.5, and 5 wt% NaCl). The study reveals the dominance of apatite dissolution textures with the formation of micron-scale etch pits and dissolution channels developing prominently along the c-axis of the apatite crystals. Backscattered electron imaging shows an increase in apatite dissolution with increased temperature and when reacting the crystals with more acidic and higher salinity starting fluids. This study also demonstrates an increase in dissolved REE in the experimental fluids corroborating with the observed apatite dissolution behavior. Backscattered electron imaging of secondary minerals formed during apatite dissolution and scanning electron microscopy-based energy dispersive spectrometer peaks for Ca, P, and REE support the formation of monazite-(Ce) and minor secondary apatite as deduced from fluid chemistry (i.e., dissolved P and REE concentrations). The studied apatite reaction textures and chemistry of the reacted fluids both indicate that the mobility of REE is controlled by the dissolution of apatite coupled with precipitation of monazite-(Ce), which are enhanced by the addition of NaCl in the starting fluids. This coupled process can be traced by comparing the REE to P ratios in the reacted fluids with the stoichiometry of the unreacted apatite crystals. Apatite metasomatized at temperatures <300 °C is therefore controlled by dissolution rather than dissolution-reprecipitation reactions commonly observed in previous experiments conducted above 300 °C. Further, this study

demonstrates that the presence of NaCl plays a crucial role in increasing the solubility of apatite, which controls the availability of REE to form secondary phosphates even in mildly acidic aqueous fluids. This implies that both the effects of acidity/alkalinity of the fluids and the role of dissolved alkalis (NaCl and KCl), need to be considered for understanding the controls on REE in magmatic-hydrothermal systems. Lastly, the experiments of this study expand the known conditions at which apatite is susceptible to be overprinted by hydrothermal alteration from 900 °C down to 150 °C and highlights the necessity of appropriately screening apatite grains using backscattered electron and cathodoluminescence imaging for signs of hydrothermal alteration textures in igneous apatite.

Keywords: Apatite, monazite, REE mobility, dissolution-precipitation, metasomatism, hydrothermal fluids, experiments

INTRODUCTION

Apatite, $Ca_5(PO_4)_3(F,OH,Cl)$ has a structure compatible to many elements, particularly the rare earth elements (REE). Its ubiquity in igneous and metamorphic rocks makes apatite an ideal tracer of petrogenetic processes (Heinrich et al. 1997; Andrehs and Heinrich 1998; Gratz and Heinrich 1998; Piccoli and Candela 2002; Spear and Pyle 2002; Harlov 2015; Hughes and Rakovan 2015; Webster and Piccoli 2015). For instance, accessory apatite has been used to identify the magma fertility of subvolcanic intrusions and their potential to host porphyry-skarn deposits (Mao et al. 2016; Gao et al. 2020; Yang et al. 2020; Cao et al. 2021; Chen et al. 2021; Liu et al. 2021). Apatite also occurs in a wide range of mineral deposits, including iron oxide apatite (IOA) deposits and carbonatites, where it can host economic levels of REE, and where its textures and chemical signatures have been used to investigate magmatic versus hydrothermal processes (Hofstra et al. 2016; Broom-Fendley et al. 2017; Duan and Jiang 2018; Andersson et al. 2019; La Cruz et al. 2019; Palma et al. 2019).

Over the past decades, several studies have established that apatite is highly susceptible to hydrothermal alteration and that the trace element signatures of this mineral may not necessarily be reflective of the original conditions of crystal growth (Broom-Fendley et al. 2016; Harlov et al. 2016; Jonsson et al. 2016; Krneta et al. 2017). The alteration of apatite is a key control on the mobility of REE in hydrothermal fluids (Uher et al. 2015; Verplanck 2017), and the trace element composition of apatite provides important insights into the nature of metasomatic processes (Harlov and Förster 2002; Harlov 2015; Krneta et al. 2016; Normandeau et al. 2018). The replacement of primary apatite by secondary REE-rich minerals such as monazite and xenotime

is common in many ore deposits (Harlov et al. 2002, 2016; Jonsson et al. 2016). A recent study from the Pea Ridge IOA-(REE) deposit in Missouri shows that apatite replacement by monazite and xenotime can occur at temperatures below 400 °C (Harlov et al. 2016). Apatite also controls REE mobility in subaerial and submarine geothermal systems (Monecke et al. 2003; Fowler et al. 2019).

Previous piston-cylinder and cold-seal experiments have provided significant insights into apatite metasomatism through the study of reaction textures and changes in mineral chemistry at temperatures between 300 and 900 °C and pressures from 100 to 2000 MPa (Ayers and Watson 1991, 1993; Brenan 1993; Harlov and Förster 2003; Harlov et al. 2005; Antignano and Manning 2008; Betkowski et al. 2016; Konecke et al. 2017; Mair et al. 2017). These studies confirm that mobilization of REE can be controlled by the coupled dissolution-reprecipitation of apatite and the formation of secondary monazite and xenotime. However, so far only a few studies have focused on apatite solubility at low temperature and its role in REE mobilization (Köhler et al. 2005; Chaïrat et al. 2007; Harouiya et al. 2007; Zhu et al. 2009). Particularly, little is known on apatite solubility in acidic and saline hydrothermal fluids at 100 to 300 °C, which are conditions that could be favorable for the formation of REE chloride complexes and REE moblization in aqueous fluids (Migdisov et al. 2009, 2016; Gysi and Williams-Jones 2013; Perry and Gysi 2020). Furthermore, experimental investigations show that rhabdophane [$REE(PO_4)\cdot nH_2O$] is the stable REE phosphate and sink for REE at temperatures below 100 °C, whereas the anhydrous REE phosphate minerals monazite and xenotime control the solubility of REE at temperatures above 100 °C (Gysi et al. 2015, 2018; Gausse et al. 2016; Ochiai and Utsunomiya 2017; Arinicheva et al. 2018; Van Hoozen et al. 2020; Gysi and Harlov 2021). Several studies have also

utilized experimentally derived thermodynamic models to calculate the Cl, OH, and F composition and solubility of apatite in aqueous fluids (Zhu and Sverjensky 1991; Mair et al. 2017), in melts, and melt-fluids (Webster et al. 2009, 2017; Li and Hermann 2015, 2017; McCubbin et al. 2015; Riker et al. 2018; Li and Costa 2020), which are supported by calorimetric experiments (Hovis and Harlov 2010; Hovis et al. 2014).

In this study, we explore the solubility of apatite in hydrothermal fluids of acidic to mildly acidic compositions (pH of 2–4) at temperatures between 100 and 250 °C and at saturated water vapor pressure. Batch type hydrothermal experiments consisted of reacting natural apatite crystals with $HClO_4$- and HCl-(NaCl)-bearing aqueous fluids to determine mineral reaction textures, and REE fluid and mineral compositional evolution upon apatite-fluid interaction. These experiments yield new insights into the controls of apatite and secondary REE phosphates on the mobility of REE as a function of pH, temperature, and fluid salinity.

METHODS

Starting Materials

Natural apatite from Durango, Mexico, was used in the batch type experiments because this fluorapatite has been extensively characterized in previous studies, which includes electron microprobe microanalysis (EMPA; Stormer et al. 1993), laser ablation-inductively coupled plasma mass spectrometry (LA-ICP-MS; Marks et al. 2012; Chew et al. 2016), Raman and infrared spectroscopy (Williams and Knittle 1996; Clark et al. 2016), and fission track dating (Jonckheere et al. 2015). As Durango apatite displays some level of core to rim compositional

heterogeneity (Chew et al. 2016), single crystals used in this study were carefully characterized using LA-ICP-MS. Several dozen, gem-quality euhedral apatite crystals ranging from 1–5 mm in size were selected by hand-picking under a binocular microscope. Cloudy grains or grains that contained inclusions were not used. All grains were cleaned at least three times in an ultrasonic bath using Milli-Q water (18.0 MΩ·cm).

The starting fluids for the batch-type experiments (Table 1) were prepared using trace metal grade $HClO_4$ (Fisher Scientific) or HCl (Fisher Scientific), which were added dropwise to 400 ml of Milli-Q water to reach pH values of 2, 3, and 4. The pH values of the starting solutions were measured at room temperature using a Metrohm unitrode with an integrated Pt1000 temperature sensor (model 6.0260.010) and a Metrohm 913 pH meter (precision of +/- 0.03 pH units and resolution of 0.01 pH units). The electrode was calibrated using commercial buffer solutions (Fisher Scientific; pH 2.00, 4.00, and 7.00; accuracy of +/-0.01). Some of the experimental solutions were spiked with REE by adding a NIST traceable certified multi-element REE standard (SCP Science) to reach a concentration of 1 ppm for each REE. To obtain variably saline starting solutions, solid NaCl (99.99 % purity, Sigma-Aldrich) was dissolved in the selected experimental fluids.

Experimental methods

Batch-type experiments were carried out in 45 ml Teflon-lined stainless-steel reactors (4744, Parr Instruments) at temperatures of 150 and 250 °C and at saturated water vapor pressure to study the partitioning of REE between apatite and the experimental fluids. Single apatite crystals were mounted into hand-made annealed Ti holders (Ti-foil, 99.7 % metal basis, Alfa Aesar), which

were then placed in 25 ml of the starting solution. The headspace for each liner was then flushed with dry N_2 gas for 5 minutes. The reactors were sealed and then placed into a furnace (Cole-Parmer, EW-33858-70). Temperature was maintained within 2.0 °C of the experimental set point and monitored with an Omega® temperature logger using a K-type thermocouple located at the center of the furnace. After 14 days, the reactors were removed from the furnace and immediately quenched in a water bath and cooled to room temperature in less than 20 minutes. The quenched fluids were separated from the apatite crystals and acidified with 2 % trace metal grade HNO_3 (Fischer Scientific). Saline fluids were further diluted with a matrix matched 2 % HNO_3 blank for REE and P analysis. Between experiments, empty Ti holders and Teflon liners were cleaned by soaking in concentrated H_2SO_4 for 48 hours, rinsed with water, followed by a 24-hour soak in Milli-Q water.

Analytical Methods

Dissolved REE and P concentrations were measured in the quenched experimental solutions using a Perkin Elmer NexION 300D quadrupole ICP-MS in the Department of Chemistry at Colorado School of Mines. Samples and standards were diluted using 2% HNO_3 (Fisher Scientific, trace metal grade) blank solutions and were mixed in-line with In and Rh solutions as internal standards (SCP Science, NIST traceable internal standard) to correct for instrumental drift. The calibration was carried out using a multi-element REE standard and P standards (SCP Science, NIST traceable certified standards). Single REE standards were used for interference corrections due to potential oxide (^{18}O and ^{16}O) formation. Analyzed samples were blank-subtracted after drift correction. The limits of detection were determined from the 3σ (standard

deviation) values of the blank, which were established by multiple measurements of the total procedural blank throughout the study and ranged between 10 and 20 ppb for P and between 5 and 10 ppt for the REE. The analytical precision of triplicate ICP-MS runs was < 3 % for P and < 1 % for the REE at the 95 % confidence level.

Backscattered electron (BSE) and cathodoluminescence (CL) images of the unreacted and reacted apatite grains were collected on a TESCAN MIRA3 LMH Schottky field-emission scanning electron microscope (SEM) in the Mineral and Materials Characterization Facility at the Department of Geology and Geological Engineering at Colorado School of Mines. The BSE images were taken using a TESCAN motorized retractable annular, single-crystal YAG BSE detector at an accelerating voltage of 10.0 kV and at a working distance of 10 mm. The CL images were acquired using a TESCAN Rainbow detector at an accelerating voltage of 7.0 kV and a working distance of 15 mm. The SEM is equipped with a Bruker XFlash® 6/30 silicon drift detector for energy-dispersive X-ray spectroscopy (EDS).

Trace element concentrations in the unreacted and reacted apatite grains were measured along profiles at the LA-ICP-MS Laboratory in the Department of Geology and Geological Engineering at Colorado School of Mines. An Applied Spectra RESOLution-SE 193 nm ArF excimer LA system equipped with a S-155 sample cell was used and coupled to an Agilent 8900 triple quadrupole ICP-MS/MS via a SQUID signal smoothing device. Ablation of apatite was carried out using a laser beam diameter of 30 μm, a laser energy of 3 J/cm^2, and a repetition rate of 5 Hz. Details of the instrumental settings are given in Appendix 1. The ablated material was carried by He gas and was mixed with Ar gas in a funnel sitting right above the sample cell. The

isotopes analyzed include: ^{35}Cl, ^{51}V, ^{55}Mn, ^{57}Fe, ^{75}As, ^{88}Sr, ^{89}Y, ^{139}La, ^{140}Ce, ^{141}Pr, ^{146}Nd, ^{147}Sm, ^{153}Eu, ^{157}Gd, ^{159}Tb, ^{163}Dy, ^{165}Ho, ^{166}Er, ^{169}Tm, ^{172}Yb, ^{175}Lu, ^{208}Pb, ^{232}Th, and ^{238}U. A dwell time of 100 milliseconds was used for ^{208}Pb and 10 milliseconds for all other isotopes. Each spot analysis involved one laser shot, followed by 15 seconds of waiting time for the aerosol to pass through the system. Then a gas blank was collected for 30 seconds, followed by 60 seconds of sample signal collection. NIST 610 glass was used as the external standard for all analyses. NIST 612 glass was analyzed to monitor the precision and accuracy of the analyses. The NIST 610 and NIST 612 were each measured twice at the beginning of each analytical session, with analysis being repeated every 15 samples to monitor instrumental drift. Data reduction was performed using the SILLS program (Guillong et al. 2008). A stoichiometric Ca concentration of 39 wt% was used as an internal standard for data reduction.

RESULTS

Rare earth element composition and zoning in unreacted Durango apatite

Cathodoluminescence imaging reveals that unreacted Durango apatite crystals show distinct growth zoning parallel and perpendicular to the c-axis (Fig. 1). Representative LA-ICP-MS compositional transects measured from core to rim are shown in Figures 2 and 3, with the corresponding elemental data listed in Table 2. The transects across the apatite crystals display variations in REE concentrations between the core and rims, both parallel and perpendicular to the c-axis. Compositionally distinct zones correspond to those identified in the CL images.

A transect perpendicular to the c-axis shows distinct oscillatory zoning (Fig. 2). Overall, the La concentrations show little variation across the apatite crystal whereas the other REE concentrations vary between the oscillatory growth zones and are relatively enriched in the core and depleted in the crystal rim. The transect parallel to the c-axis shows that the La concentrations decrease from ~5000 ppm in the core to ~3600 ppm in the rim, whereas the concentrations of Nd to Lu increase from core to rim (Fig. 3). The distribution of Ce differs from the other REE. Despite the REE zoning in the apatite crystals, average core and rim REE concentrations and their standard deviations indicate limited variability in the REE contents (Table 2).

Reaction textures in apatite

Apatite crystals reacted in HCl and $HClO_4$ solutions with initial pH values ranging from 2 to 4 and temperatures of 150 and 250 °C display a range of reaction textures (Fig. 4). Experiments conducted at 150 °C display <1 μm-sized etch pits along the apatite crystal surfaces (Fig. 4a). In contrast, experiments conducted at 250 °C display large etch pits extending up to ~50 μm into the reacted crystals, with many of the etch pits containing acicular secondary REE phosphates. At constant temperature (250 °C), the dissolution textures were more prominent at lower pH values, as evidenced by the larger size and increased abundance of etch pits (Fig. 4b–d).

Addition of 0.5 to 5 wt% NaCl to the starting experimental fluids doped with 1 ppm REE caused an overall increase in apatite dissolution at pH between 3 and 4 (Figs. 5, 6) in comparison to the experiments run without NaCl in the starting fluids (Fig. 4). Preferential etching along

dissolution channels following the c-axis can be observed in the apatite crystals with etch pits extending up to ~20–50 μm into the crystals (Figs. 4d, 5b, 5d, 6b). The most extensive etching and abundance of secondary REE phosphates formed in fluids containing 5 wt% NaCl (Fig. 6).

Secondary REE phosphate minerals

Small (<5 μm), secondary REE-rich minerals occur in etch pits and dissolution channels in the reacted apatite crystals (Fig. 7). Table 1 summarizes the phases identified in each experiment. Due to the small size of the crystals (<5 μm) quantitative analysis via EMPA was not feasible. Semi-quantitative SEM-EDS analyses indicate that these phases are La-, Ce-, and Nd-rich phosphate minerals (Fig. 7), stoichiometrically corresponding most closely to monazite-(Ce) and possibly REE-rich apatite. The morphology of these secondary monazite-(Ce) phases ranges from euhedral crystals to subhedral or anhedral aggregates. Small rosettes occur which may have formed because of twinning.

Apatite reacted at 150 °C contains mostly secondary monazite-(Ce) whereas in one experiment (Ap150_4) secondary apatite was identified as a possible phase because of the presence of a Ca SEM-EDS peak. Apatite reacted at 250 °C also contains both secondary monazite-(Ce) and REE-rich apatite. Element concentrations measured in the mixed monazite-(Ce) and possibly secondary apatite intergrowths typically range from 4.8 to 45.5 wt% Ca and from 4.3 to 31.7 wt% Ce.

Fluid chemistry

Measurement of the chemistry of the reacted fluids (Table 3) provides constraints on the degree of apatite dissolution and secondary phosphate mineral precipitation as each contribute to the total REE and P concentrations in the reacted fluids. Dissolved P concentrations do not show a clear relationship to temperature, while P concentrations tend to increase with decreasing pH and increasing salinity (Fig. 8a). The highest dissolved P concentrations of 165 and 184 ppm are found in the two experiments conducted at a pH of 2 and a temperature of 250 °C (Fig. 8a). In the experiments conducted with a starting fluid having a salinity of 5 wt% NaCl, a decrease in pH from 4 to 3 results in an increase in P concentrations from 24 to 62 ppm at 150 °C and 17 to 105 ppm at 250 °C.

The dissolved light (L)REE concentrations (i.e., La and Ce) display a dependence on temperature, pH, and salinity (Fig. 8b–c). In the experiments conducted with 0 wt% NaCl, the highest LREE concentrations are found in the experiments with a starting pH of 2, which are also the experiments that were observed to contain the highest dissolved P concentrations (Fig. 8a). The dissolved heavy (H)REE concentrations (i.e., Tb, Ho, and Er) display a more pronounced dependence on temperature and pH with an increase in salinity of the experimental fluids (Fig. 8d–f). In experiments conducted with 0 wt% NaCl, the dissolved HREE display similar concentrations at pH 2 as the experiments conducted at a pH of 3 and 4. In contrast, the experiments conducted with 0.5 and 5 wt% NaCl display an increase in HREE concentrations when comparing the experiments at pH 3 and 4 at both 150 and 250 °C.

Comparison of P and REE concentrations between experiments with a salinity of 0.5 and 5 wt% NaCl, permits identifying whether the REE remained in solution despite the increased apatite dissolution (Fig. 8). In all experiments, even the ones initially doped with REE concentrations, both the LREE and HREE decreased significantly upon reaction with apatite and increased salinity. For example, La values in the reacted fluids range between 41 and 579 ppb at 250 °C and between 25 and 147 ppb at 150 °C, indicating significant precipitation of REE into secondary REE phosphates. Further comparison between experiments conducted at 150 and 250 °C and a pH of 3 show that increasing the initial NaCl concentration from 0.5 to 5 wt% results in considerable decrease of dissolved REE concentrations. This behavior indicates an overall higher potential for REE precipitation into secondary phosphates which is coupled to the higher P availability due to an increase in apatite dissolution.

Mass balance calculations

Mass balance calculations were carried out based on the average of measured REE concentrations in the unreacted apatite rims listed in Table 2 and the measured REE and P concentrations measured in the reacted fluids listed in Table 3. These results indicate whether apatite dissolves stoichiometrically or if a change in REE/P ratios in the experimental fluids can be explained by the precipitation of secondary REE phosphate minerals such as monazite-(Ce) and/or apatite as observed in some of the experiments (Figs. 5–7). To evaluate these trends graphically, the molar REE/P ratios were calculated for both the fluid and apatite (Table 4). A $(REE/P)_{fluid}/(REE/P)_{apatite}$ of unity, indicates stoichiometric apatite dissolution, a ratio below 1 indicates potential REE precipitation into monazite-(Ce) or REE-rich apatite, and a ratio above 1

indicates the formation of secondary apatite. The resulting calculations are shown in Figures 9 and 10.

Figure 9a illustrates that at pH 3 many of the LREE plot below the stoichiometric line indicating potential precipitation of secondary monazite-(Ce). A comparison between experiments carried out at 150 and 250 °C further indicates that temperature had a minimal effect on the $(REE/P)_{fluid}/(REE/P)_{apatite}$ ratio for most REE, with a few HREE (Tb, Ho, Tm, and Lu) plotting above the stoichiometric line. This trend indicates that most LREE were precipitated into secondary REE phosphates, whereas the HREE remained mobile in the aqueous fluid.

Figure 9b shows the effects of pH on the $(REE/P)_{fluid}/(REE/P)_{apatite}$ ratio at 250 °C. At pH values of 2, 3, and 4, the $(REE/P)_{fluid}/(REE/P)_{apatite}$ ratios for selected LREE (La, Ce, Pr, Nd, and Sm) remained below 1, indicating that these REE precipitated into monazite-(Ce). This result is supported by the observed formation of secondary monazite-(Ce) in etch pits (Figs. 4b-d). In contrast, the $(REE/P)_{fluid}/(REE/P)_{apatite}$ ratios for other REE (i.e., Eu to Lu minus Er, Yb, and Y) plot close to the stoichiometric apatite dissolution line at pH of 2 and display a stepped increase in REE/P ratio from pH of 2 to 4. The highest $(REE/P)_{fluid}/(REE/P)_{apatite}$ ratios were observed for experiments with a starting pH of 4, indicating an increase in P precipitation into secondary REE-poor phase (possibly apatite) with an increase in pH, and a preference for the HREE to remain in the aqueous fluid.

Addition of 0.5 and 5 wt% NaCl in the starting experimental fluids doped with 1 ppm REE resulted in an overall shift for most of the REE, with $(REE/P)_{fluid}/(REE/P)_{apatite}$ ratios plotting

close to, or above, the stoichiometric apatite dissolution line (Fig. 10). This observation is also confirmed by BSE imaging which shows an increase in etching and formation of secondary REE phosphates (see Figs. 5a vs. 6a). Comparison between experiments conducted at 150 and 250 °C in saline aqueous fluids (Fig. 10a–b), further indicates that an increase in temperature results in an overall increase in REE mobility coupled with a decrease in P concentrations. This is reflected by $(REE/P)_{fluid}/(REE/P)_{apatite}$ ratios plotting preferentially above the stoichiometric apatite dissolution line. Increasing NaCl concentrations of the experiments from 0.5 to 5 wt% results in a distinct decrease in $(REE/P)_{fluid}/(REE/P)_{apatite}$ ratios for LREE and indicates a higher potential for saturation of secondary REE phosphates.

DISCUSSION

Control of apatite metasomatism on REE mobility in hydrothermal fluids

Previous experimental work in cold seal pressure vessels and/or piston cylinder apparatus conducted at temperatures between 300 and 900 °C and pressures of 500 and 2000 MPa were aimed at investigating the controls of fluid chemistry on fluid-induced coupled dissolution and reprecipitation processes associated with metasomatism of Durango apatite (Harlov and Förster 2003; Harlov et al. 2005; Antignano and Manning 2008). Experiments by Harlov and Förster (2003) and Harlov et al. (2005) showed that metasomatism of apatite is affected by addition of HCl, H_2SO_4, and alkali salts (NaCl, KCl, and $CaCl_2$). In these high pressure-temperature experiments, apatite metasomatism is characterized by several features including: 1) the formation of monazite inclusions within or on the surface of the reacted apatite crystals (300 – 900 °C); 2) suppression of monazite formation in H_2O+NaCl and H_2O+$CaCl_2$ vs. H_2O+KCl-

bearing fluids; 3) the formation of distinct apatite zones of REE-enrichment/-depletion which can be observed in BSE imaging. The enhancement of Durango apatite solubility by addition of NaCl was also observed in the piston-cylinder experiments by Antignano and Manning (2008) conducted at 700 – 900 °C and 0.7 to 2.0 GPa. This study showed that, while pressure and temperature increased apatite solubility in pure H_2O, addition of NaCl increased the apatite solubility more considerably and that apatite dissolves incongruently to form monazite plus dissolved solutes in the fluid (Antignano and Manning 2008).

Our experimental results agree with previous work regarding the increase in solubility of apatite with increasing NaCl content and decreasing pH of the starting fluids. Based on the observed apatite dissolution textures (Figs. 4–7) and fluid chemistry (Figs. 8–10), we conclude the following points from our experimental work between 150–250 °C: 1) acidic fluids (pH of 2) promote apatite dissolution reflected by stoichiometric REE/P ratios in both apatite and fluid; 2) mildly acidic fluids (pH of 3–4) decrease apatite solubility and promote precipitation of monazite-(Ce); 3) addition of NaCl increases apatite solubility with the formation of monazite-(Ce) promoted at lower temperature and an increased REE mobility at higher temperature in saline fluids. Overall, experiments with fluids having an initial salinity of 0.5 and 5 wt% NaCl showed the most extensive alteration of apatite, which is evidenced by a higher abundance of etch pits around the crystal and deeper penetration into the apatite grain preferentially along the c-axis (Figs. 5, 6). Harlov et al. (2005) also observed numerous sub-parallel dissolution nano-channels in which secondary monazite formed, which is similar to what is observed in our experiments but at the micron-scale (Figs. 4–7). In contrast to the high temperature-pressure experiments discussed above, the reacted apatite in our experiments were dominated by

dissolution textures and no clear zoning was observed in BSE or CL that would suggest a control by apatite dissolution-reprecipitation processes. Our experiments suggest that between 150–250 °C, the mobility of REE is controlled by the solubility behavior of apatite which limits the availability of REE and P to form secondary monazite-(Ce) on the crystal surfaces.

The stability of monazite and aqueous REE complexes in hydrothermal fluids

A recent series of hydrothermal monazite and xenotime solubility experiments conducted in acidic fluids between 100 and 250 °C indicate that the REE phosphates display a retrograde solubility (Gysi et al. 2015, 2018; Van Hoozen et al. 2020; Gysi and Harlov 2021). In contrast, our experimental fluids reacted with apatite indicate an increase in dissolved REE concentrations with an increase in temperature from 150 to 250 °C (Fig. 8). Comparison of the REE/P ratios in apatite and fluid in the experiments with 0.5 and 5 wt. % NaCl further indicate that the formation of monazite-(Ce) is favored at 150 °C over experiments conducted at 250 °C (Fig. 10). This behavior can be explained by the formation of aqueous chloride complexes in saline aqueous fluids used in our experiments, that further enhance the solubility of REE phosphates according to:

$$(1)\ REEPO_4\ (monazite) = REE^{3+} + PO_4^{3-}$$

$$(2)\ REE^{3+} + Cl^- = REECl^{2+}$$

Speciation experiments by Migdisov et al. (2009) and thermodynamic modeling by Gysi and Williams-Jones (2013), Migdisov and Williams-Jones (2014) as well as Perry and Gysi (2018)

indicate that REE solubility in saline aqueous fluids increases with temperatures due to an increased stability of REE chloride complexes at >150–350 °C. This behavior indicates that in saline aqueous fluids the formation of aqueous REE chloride competes with the precipitation of REE and P into monazite-(Ce) under hydrothermal conditions up to 350 °C. Based on our experimental results in acidic to mildly acidic fluids, we conclude that in H_2O-HCl-bearing fluids the apatite solubility is relatively low and the REE precipitate mostly into monazite-(Ce). In contrast, experiments conducted in H_2O-HCl-NaCl-bearing fluids indicate a considerable increase in apatite solubility and mobility of REE in comparison to the NaCl-free experiments.

IMPLICATIONS

High-temperature metasomatism of apatite and REE mobility is closely related to the stability of both monazite and xenotime in natural systems. Examples of apatite-monazite-xenotime mineral paragenesis have been described in IOA deposits such as the Grängesberg mining district in Bergslagen, Sweden (Jonsson et al. 2016) and Pea Ridge in Missouri, USA (Harlov et al. 2016). In contrast to these high temperature systems, the alteration of apatite in low temperature aqueous fluids (<300 °C) does not appear to be controlled by dissolution-reprecipitation of apatite. In the experiments conducted here, no reaction fronts were observed in the reacted apatite crystals. These observations suggest that low-temperature alteration of igneous apatite may be difficult to observe in natural systems because the alteration of apatite is mainly dissolution controlled under acidic to mildly acidic conditions. Nevertheless, subsequent pH neutralization and/or saturation of apatite by addition of Ca and P to the fluid can lead to precipitation of secondary apatite, which is likely distinguishable from primary igneous apatite

crystals not dissolved during metasomatism. The significant apatite dissolution textures, such as micron-scale etch pits in the low temperature experiments, can be related to the increased dissociation of acids (e.g., $HCl_{(aq)} = H^+ + Cl^-$) at low temperature and the formation of chloride complexes (Eqs. 1–2) with increased salinity of the fluids. The experiments of this study expand the known conditions at which apatite is susceptible to be overprinted by hydrothermal alteration from 900 °C (Harlov and Förster 2003) down to 150 °C (this study). This implies that apatite alteration can occur in various geologic environments and that the original igneous signature of apatite may not necessarily be preserved in igneous rocks that have been affected by subsolidus hydrothermal alteration. This highlights the necessity of appropriately screening apatite grains using BSE and CL imaging for signs of hydrothermal alteration textures if the goal is to use the geochemical signature of apatite to infer magma petrogenesis or magmatic fertility of igneous rocks (Bouzari et al. 2016). The present contribution further highlights how apatite can control the budget and mobility of REE in fluids which are acidic and saline at temperatures <300 °C. Fluids of similar nature appear to be important in the late stage REE-enrichment in carbonatite REE deposits such as Songwe Hill in Malawi (Broom-Fendley et al. 2017) and certain IOA deposits such as Pea Ridge in Missouri (Harlov et al. 2016; Hofstra et al. 2016).

ACKNOWLEDGMENTS

We thank K. Challis and J. Ranville for help provided during ICP-MS analyses and K. Pfaff for assistance during SEM imaging. This project was supported by a grant from the National Science Foundation to APG (NSF CAREER grant EAR-2039674). Acquisition of the SEM-CL detector used in this study was supported by the National Science Foundation to TM (NSF grant

1822197). We are grateful for the constructive comments by Justin Casaus and an anonymous reviewer. We thank Associate Editor D. Harlov for handling this manuscript. We are honored to participate in this special issue for Jim Webster, and extend our deepest respect for his contributions to science.

REFERENCES CITED

Andersson, S.S., Wagner, T., Jonsson, E., Fusswinkel, T., and Whitehouse, M.J. (2019) Apatite as a tracer of the source, chemistry and evolution of ore-forming fluids: The case of the Olserum-Djupedal REE-phosphate mineralisation, SE Sweden. Geochimica et Cosmochimica Acta, 255, 163–187.

Andrehs, G., and Heinrich, W. (1998) Experimental determination of REE distributions between monazite and xenotime: Potential for temperature-calibrated geochronology. Chemical Geology, 149, 83–96.

Antignano, A., and Manning, C.E. (2008) Fluorapatite solubility in H_2O and H_2O-NaCl at 700 to 900 °C and 0.7 to 2.0 GPa. Chemical Geology, 251, 112–119.

Arinicheva, Y., Gausse, C., Neumeier, S., Brandt, F., Rozov, K., Szenknect, S., Dacheux, N., Bosbach, D., and Deissmann, G. (2018) Influence of temperature on the dissolution kinetics of synthetic $LaPO_4$-monazite in acidic media between 50 and 130 °C. Journal of Nuclear Materials, 509, 488–495.

Ayers, J.C., and Watson, E.B. (1991) Solubility of apatite, monazite, zircon, and rutile in supercritical aqueous fluids with implications for subduction zone geochemistry. Philosophical Transactions of the Royal Society of London, Series A: Physical and Engineering Sciences, 335, 365–375.

——— (1993) Apatite/fluid partitioning of rare-earth elements and strontium: Experimental results at 1.0 GPa and 1000 °C and application to models of fluid-rock interaction. Chemical Geology, 110, 299–314.

Betkowski, W.B., Harlov, D.E., and Rakovan, J.F. (2016) Hydrothermal mineral replacement reactions for an apatite-monazite assemblage in alkali-rich fluids at 300–600 °C and 100 MPa. American Mineralogist, 101, 2620–2637.

Bouzari, F., Hart, C.J.R., Bissig, T., and Barker, S. (2016) Hydrothermal alteration revealed by apatite luminescence and chemistry: A potential indicator mineral for exploring covered porphyry copper deposits. Economic Geology, 111, 1397–1410.

Brenan, J.M. (1993) Partitioning of fluorine and chlorine between apatite and aqueous fluids at high pressure and temperature: Implications for the F and Cl content of high P-T fluids. Earth and Planetary Science Letters, 117, 251–263.

Broom-Fendley, S., Styles, M.T., Appleton, J.D., Gunn, G., and Wall, F. (2016) Evidence for dissolution-reprecipitation of apatite and preferential LREE mobility in carbonatite-derived late-stage hydrothermal processes. American Mineralogist, 101, 596–611.

Broom-Fendley, S., Brady, A.E., Wall, F., Gunn, G., and Dawes, W. (2017) REE minerals at the Songwe Hill carbonatite, Malawi: HREE-enrichment in late-stage apatite. Ore Geology Reviews, 81, 23–41.

Cao, M.J., Evans, N.J., Hollings, P., Cooke, D.R., McInnes, B.I.A., and Qin, K.Z. (2021) Apatite texture, composition, and O-Sr-Nd isotope signatures record magmatic and hydrothermal fluid characteristics at the Black Mountain porphyry deposit, Philippines. Economic Geology, 116, 1189–1207.

Chaïrat, C., Schott, J., Oelkers, E.H., Lartigue, J.E., and Harouiya, N. (2007) Kinetics and mechanism of natural fluorapatite dissolution at 25 °C and pH from 3 to 12. Geochimica et Cosmochimica Acta, 71, 5901–5912.

Chen, X., Leng, C.B., Zou, S., Li, K., and Zhang, L. (2021) Geochemical compositions of apatites from the Xuejiping and Disuga porphyries in Zhongdian arc: Implications for porphyry Cu mineralization. Ore Geology Reviews, 130, 103954.

Chew, D.M., Babechuk, M.G., Cogné, N., Mark, C., O'Sullivan, G.J., Henrichs, I.A., Doepke, D., and McKenna, C.A. (2016) (LA,Q)-ICPMS trace-element analyses of Durango and McClure Mountain apatite and implications for making natural LA-ICPMS mineral standards. Chemical Geology, 435, 35–48.

Clark, K., Zhang, Y., and Naab, F.U. (2016) Quantification of CO_2 concentration in apatite. American Mineralogist, 101, 2443–2451.

Duan, D.F., and Jiang, S.Y. (2018) Using apatite to discriminate synchronous ore-associated and barren granitoid rocks: A case study from the Edong metallogenic district, South China. Lithos, 310–311, 369–380.

Fowler, A.P.G., Zierenberg, R.A., Reed, M.H., Palandri, J., Óskarsson, F., and Gunnarsson, I. (2019) Rare earth element systematics in boiled fluids from basalt-hosted geothermal systems. Geochimica et Cosmochimica Acta, 244, 129–154.

Gao, X., Yang, L., Wang, C., He, W., Bao, X., and Zhang, S. (2020) Halogens and trace elements of apatite from Late Mesozoic and Cenozoic porphyry Cu-Mo-Au deposits in SE Tibet, China: Constraints on magmatic fertility and granitoid petrogenesis. Journal of Asian Earth Sciences, 203, 104552.

Gausse, C., Szenknect, S., Qin, D.W., Mesbah, A., Clavier, N., Neumeier, S., Bosbach, D., and Dacheux, N. (2016) Determination of the solubility of rhabdophanes $LnPO_4 \cdot 0.667H_2O$ (Ln = La to Dy). European Journal of Inorganic Chemistry, 2016, 4615–4630.

Gratz, R., and Heinrich, W. (1998) Monazite-xenotime thermometry. III. Experimental calibration of the partitioning of gadolinium between monazite and xenotime. European Journal of Mineralogy, 10, 579–588.

Guillong, M., Meier, D.L., Allan, M.M., Heinrich, C.A., and Yardley, B.W. (2008). SILLS: A MATLAB-based program for the reduction of laser ablation ICP-MS data of homogeneous materials and inclusions. Mineralogical Association of Canada Short Course, 40, 328–333.

Gysi, A.P., and Harlov, D. (2021) Hydrothermal solubility of $TbPO_4$, $HoPO_4$, $TmPO_4$, and $LuPO_4$ xenotime endmembers at pH of 2 and temperatures between 100 and 250 °C. Chemical Geology, 567, 120072.

Gysi, A.P., and Williams-Jones, A.E. (2013) Hydrothermal mobilization of pegmatite-hosted REE and Zr at Strange Lake, Canada: A reaction path model. Geochimica et Cosmochimica Acta, 122, 324–352.

Gysi, A.P., Williams-Jones, A.E., and Harlov, D. (2015) The solubility of xenotime-(Y) and other HREE phosphates ($DyPO_4$, $ErPO_4$ and $YbPO_4$) in aqueous solutions from 100 to 250 °C and psat. Chemical Geology, 401, 83–95.

Gysi, A.P., Harlov, D., and Miron, G.D. (2018) The solubility of monazite ($CePO_4$), $SmPO_4$, and $GdPO_4$ in aqueous solutions from 100 to 250 °C. Geochimica et Cosmochimica Acta, 242, 143–164.

Harlov, D.E. (2015) Apatite: A fingerprint for metasomatic processes. Elements, 11, 171–176.

Harlov, D.E., and Förster, H.J. (2002) High-grade fluid metasomatism on both a local and a regional scale: The Seward Peninsula, Alaska, and the Val Strona di Omegna, Ivrea–Verbano Zone, northern Italy. Part II: Phosphate mineral chemistry. Journal of Petrology, 43, 801–824.

——— (2003) Fluid-induced nucleation of (Y+REE)-phosphate minerals within apatite: Nature and experiment. Part II. Fluorapatite. American Mineralogist, 88, 1209–1229.

Harlov, D.E., Andersson, U. B., Förster, H.-J., Nyström, J.O., Dulski, P., and Broman, C. (2002) Apatite – monazite relations in the Kiirunavaara magnetite–apatite ore, northern Sweden. Chemical Geology, 191, 47–72.

Harlov, D.E., Wirth, R., and Förster, H.J. (2005) An experimental study of dissolution-reprecipitation in fluorapatite: Fluid infiltration and the formation of monazite. Contributions to Mineralogy and Petrology, 150, 268–286.

Harlov, D.E., Meighan, C.J., Kerr, I.D., and Samson, I.M. (2016) Mineralogy, chemistry, and fluid-aided evolution of the Pea Ridge Fe oxide-(Y + REE) deposit, southeast Missouri, USA. Economic Geology, 111, 1963–1984.

Harouiya, N., Chaïrat, C., Köhler, S.J., Gout, R., and Oelkers, E.H. (2007) The dissolution kinetics and apparent solubility of natural apatite in closed reactors at temperatures from 5 to 50 °C and pH from 1 to 6. Chemical Geology, 244, 554–568.

Heinrich, W., Andrehs, G., and Franz, G. (1997) Monazite-xenotime miscibility gap thermometry. I. An empirical calibration. Journal of Metamorphic Geology, 15, 3–16.

Hofstra, A.H., Meighan, C.J., Song, X., Samson, I., Marsh, E.E., Lowers, H.A., Emsbo, P., and Hunt, A.G. (2016) Mineral thermometry and fluid inclusion studies of the Pea Ridge iron

oxide-apatite-rare earth element deposit, Mesoproterozoic St. Francois Mountains Terrane, southeast Missouri, USA. Economic Geology, 111, 1985–2016.

Hovis, G.L., and Harlov, D.E. (2010) Solution calorimetric investigation of fluor-chlorapatite crystalline solutions. American Mineralogist, 95, 946–952.

Hovis, G.L., McCubbin, F.M., Nekvasil, H., Ustunisik, G., Woerner, W.R., and Lindsley, D.H. (2014) A novel technique for fluorapatite synthesis and the thermodynamic mixing behavior of F-OH apatite crystalline solutions. American Mineralogist, 99, 890–897.

Hughes, J.M., and Rakovan, J.F. (2015) Structurally robust, chemically diverse: Apatite and apatite supergroup minerals. Elements, 11, 165–170.

Jonckheere, R., Van den haute, P., and Ratschbacher, L. (2015) Standardless fission-track dating of the Durango apatite age standard. Chemical Geology, 417, 44–57.

Jonsson, E., Harlov, D.E., Majka, J., Högdahl, K., and Persson-Nilsson, K. (2016) Fluorapatite-monazite-allanite relations in the Grängesberg apatite-iron oxide ore district, Bergslagen, Sweden. American Mineralogist, 101, 1769–1782.

Köhler, S.J., Harouiya, N., Chaïrat, C., and Oelkers, E.H. (2005) Experimental studies of REE fractionation during water-mineral interactions: REE release rates during apatite dissolution from pH 2.8 to 9.2. Chemical Geology, 222, 168–182.

Konecke, B.A., Fiege, A., Simon, A.C., and Holtz, F. (2017) Cryptic metasomatism during late-stage lunar magmatism implicated by sulfur in apatite. Geology, 45, 739–742.

Krneta, S., Ciobanu, C.L., Cook, N.J., Ehrig, K., and Kontonikas-Charos, A. (2016) Apatite at Olympic Dam, South Australia: A petrogenetic tool. Lithos, 262, 470–485.

——— (2017) Rare earth element behaviour in apatite from the Olympic Dam Cu–U–Au–Ag deposit, South Australia. Minerals, 7, 135.

La Cruz, N.L., Simon, A.C., Wolf, A.S., Reich, M., Barra, F., and Gagnon, J.E. (2019) The geochemistry of apatite from the Los Colorados iron oxide–apatite deposit, Chile: Implications for ore genesis. Mineralium Deposita, 54, 1143–1156.

Li, W., and Costa, F. (2020) A thermodynamic model for F-Cl-OH partitioning between silicate melts and apatite including non-ideal mixing with application to constraining melt volatile budgets. Geochimica et Cosmochimica Acta, 269, 203–222.

Li, H., and Hermann, J. (2015) Apatite as an indicator of fluid salinity: An experimental study of chlorine and fluorine partitioning in subducted sediments. Geochimica et Cosmochimica Acta, 166, 267–297.

——— (2017) Chlorine and fluorine partitioning between apatite and sediment melt at 2.5 GPa, 800 °C: A new experimentally derived thermodynamic model. American Mineralogist, 102, 580–594.

Liu, M.Y., Zhou, M.F., Su, S.G., and Chen, X.G. (2021) Contrasting geochemistry of apatite from peridotites and sulfide ores of the Jinchuan Ni-Cu sulfide deposit, NW China. Economic Geology, 116, 1073–1092.

Mair, P., Tropper, P., Harlov, D.E., and Manning, C.E. (2017) The solubility of apatite in H_2O, KCl-H_2O, NaCl-H_2O at 800 °C and 1.0 GPa: Implications for REE mobility in high-grade saline brines. Chemical Geology, 470, 180–192.

Mao, M., Rukhlov, A. S., Rowins, S. M., Spence, J., and Coogan, L.A. (2016) Apatite trace element compositions : A robust new tool for mineral exploration. Economic Geology, 111, 1187–1222.

Marks, M.A.W., Wenzel, T., Whitehouse, M.J., Loose, M., Zack, T., Barth, M., Worgard, L., Krasz, V., Eby, G.N., Stosnach, H., and Markl, G. (2012) The volatile inventory (F, Cl, Br,

S, C) of magmatic apatite: An integrated analytical approach. Chemical Geology, 291, 241–255.

McCubbin, F.M., Vander Kaaden, K.E., Tartèse, R., Boyce, J.W., Mikhail, S., Whitson, E.S., Bell, A.S., Anand, M., Franchi, I.A., Wang, J.H., and Hauri, E.H. (2015) Experimental investigation of F, Cl, and OH partitioning between apatite and Fe-rich basaltic melt at 1.0–1.2 GPa and 950–1000 °C. American Mineralogist, 100, 1790–1802.

Migdisov, A.A., and Williams-Jones, A.E. (2014) Hydrothermal transport and deposition of the rare earth elements by fluorine-bearing aqueous liquids. Mineralium Deposita 49, 987–997.

Migdisov, A.A., Williams-Jones, A.E., and Wagner, T. (2009) An experimental study of the solubility and speciation of the rare earth elements (III) in fluoride- and chloride-bearing aqueous solutions at temperatures up to 300 °C. Geochimica et Cosmochimica Acta 73, 7087–7109.

Migdisov, A., Williams-Jones, A.E., Brugger, J., and Caporuscio, F.A. (2016) Hydrothermal transport, deposition, and fractionation of the REE: Experimental data and thermodynamic calculations. Chemical Geology, 439, 13–42.

Monecke, T., Herzig, P.M., Kempe, U., and Dulski, P. (2003) Rare earth element mobility during hydrothermal alteration in the footwall of the Waterloo VHMS deposit, Australia. In D. Eliopoulos et al., Eds., Proceedings of the 7th Biennial SGA meeting, p. 163–166, Millpress, Rotterdam.

Normandeau, P.X., Harlov, D.E., Corriveau, L., Paquette, J., and McMartin, I. (2018) Characterization of fluorapatite within iron oxide alkali-calcic alteration systems of the

Great Bear magmatic zone: A potential metasomatic process record. Canadian Mineralogist, 56, 167–187.

Ochiai, A., and Utsunomiya, S. (2017) Crystal chemistry and stability of hydrated rare-earth phosphates formed at room temperature. Minerals, 7, 84.

Palma, G., Barra, F., Reich, M., Valencia, V., Simon, A.C., Vervoort, J., Leisen, M., and Romero, R. (2019) Halogens, trace element concentrations, and Sr-Nd isotopes in apatite from iron oxide-apatite (IOA) deposits in the Chilean iron belt: Evidence for magmatic and hydrothermal stages of mineralization. Geochimica et Cosmochimica Acta, 246, 515–540.

Perry, E.P., and Gysi, A.P. (2018) Rare earth elements in mineral deposits: Speciation in hydrothermal fluids and partitioning in calcite. Geofluids, 2018, 5382480.

——— (2020) Hydrothermal calcite-fluid REE partitioning experiments at 200 °C and saturated water vapor pressure. Geochimica et Cosmochimica Acta, 286, 177–197.

Piccoli, P.M., and Candela, P.A. (2002) Apatite in igneous systems. Reviews in Mineralogy and Geochemistry, 48, 255–292.

Riker, J., Humphreys, M.C.S., Brooker, R.A., and De Hoog, J.C.M. (2018) First measurements of OH-C exchange and temperature-dependent partitioning of OH and halogens in the system apatite-silicate melt. American Mineralogist, 103, 260–270.

Spear, F.S., and Pyle, J.M. (2002) Apatite, monazite, and xenotime in metamorphic rocks. Reviews in Mineralogy and Geochemistry, 48, 293–335.

Stormer, J.C., Jr., Pierson, M.L., and Tacker, R.C. (1993) Variation of F and Cl X-ray intensity due to anisotropic diffusion in apatite during electron microprobe analysis. American Mineralogist, 78, 641–648.

Uher, P., Ondrejka, M., Bačík, P., Broska, I., and Konečný, P. (2015) Britholite, monazite, REE carbonates, and calcite: Products of hydrothermal alteration of allanite and apatite in A-type granite from Stupné, Western Carpathians, Slovakia. Lithos, 236–237, 212–225.

Van Hoozen, C.J., Gysi, A.P., and Harlov, D.E. (2020) The solubility of monazite ($LaPO_4$, $PrPO_4$, $NdPO_4$, and $EuPO_4$) endmembers in aqueous solutions from 100 to 250 °C. Geochimica et Cosmochimica Acta, 280, 302–316.

Verplanck, P.L. (2017) The role of fluids in the formation of rare earth element deposits. Procedia Earth and Planetary Science, 17, 758–761.

Webster, J.D., and Piccoli, P.M. (2015) Magmatic apatite: A powerful, yet deceptive, mineral. Elements, 11, 177–182.

Webster, J.D., Tappen, C.M., and Mandeville, C.W. (2009) Partitioning behavior of chlorine and fluorine in the system apatite–melt–fluid. II: Felsic silicate systems at 200 MPa. Geochimica et Cosmochimica Acta, 73, 559–581.

Webster, J.D., Goldoff, B.A., Flesch, R.N., Nadeau, P.A., and Silbert, Z.W. (2017) Hydroxyl, Cl, and F partitioning between high-silica rhyolitic melts-apatite-fluid(s) at 50–200 MPa and 700–1000 °C. American Mineralogist, 102, 61–74.

Williams, Q., and Knittle, E. (1996) Infrared and Raman spectra of $Ca_5(PO_4)_3F_2$-fluorapatite at high pressures: Compression-induced changes in phosphate site and Davydov splittings. Journal of Physics and Chemistry of Solids, 57, 417–422.

Yang, F., Santosh, M., Glorie, S., Xue, F., Zhang, S., and Zhang, X. (2020) Apatite geochronology and chemistry of Luanchuan granitoids in the East Qinling Orogen, China: Implications for petrogenesis, metallogenesis and exploration. Lithos, 378–379, 105797.

Zhu, C., and Sverjensky, D.A. (1991) Partitioning of F-Cl-OH between minerals and hydrothermal fluids. Geochimica et Cosmochimica Acta, 55, 1837–1858.

Zhu, Y., Zhang, X., Chen, Y., Xie, Q., Lan, J., Qian, M., and He, N. (2009) A comparative study on the dissolution and solubility of hydroxylapatite and fluorapatite at 25 °C and 45 °C. Chemical Geology, 268, 89–96.

TABLE 1. Experimental starting conditions of the apatite-fluid batch-type experiments and secondary REE phosphates identified.

Experiment	*T* (°C)	$pH_{25\,°C}$	$HClO_4$ (mol/kg)	HCl (mol/kg)	NaCl (wt%)	REE (ppm)	Secondary REE minerals
Ap150_1	150	3	-	0.001	-	-	monazite-(Ce)
Ap150_2_REE	150	3	-	0.001	0.5	1	monazite-(Ce)
Ap150_3_REE	150	3	-	0.001	5	1	monazite-(Ce)
Ap150_4	150	4	-	0.0001	-	-	monazite-(Ce), apatite
Ap150_5_REE	150	4	-	0.0001	0.5	1	monazite-(Ce)
Ap150_6_REE	150	4	-	0.0001	5	1	monazite-(Ce)
Ap250_1	250	2	0.01		-	-	monazite-(Ce)
Ap250_2	250	2	0.01		-	-	monazite-(Ce)
Ap250_3	250	3	-	0.001	-	-	monazite-(Ce)
Ap250_4_REE	250	3	-	0.001	0.5	1	monazite-(Ce)
Ap250_5_REE	250	3	-	0.001	5	1	monazite-(Ce)
Ap250_6	250	4	0.0001	-	-	-	-
Ap250_8_REE	250	4	0.0001	-	-	1	monazite-(Ce), apatite
Ap250_9_REE	250	4	-	0.0001	0.5	1	monazite-(Ce)
Ap250_10_REE	250	4	-	0.0001	5	1	monazite-(Ce), apatite
Ap250_11	250	4	-	0.0001	-	-	-

TABLE 2. LA-ICP-MS analyses of unreacted apatite showing data for core and rim analyses (n= 10 spots).

Element	Durango_A (Core)	σ	Durango_A (Rim)	σ	Durango_B (Core)	σ	Durango_B (Rim)	σ
Cl (ppm)	1,310	*40*	1,240	*50*	1,550	*50*	1,400	*80*
V	37.4	*1.4*	20.3	*2.9*	58.9	*1.3*	29.9	*5.5*
Mn	100	*1*	97.6	*1.2*	103	*1*	101	*2*
Fe	278	*5*	304	*9*	287	*7*	290	*9*
As	1,050	*50*	665	*127*	1,570	*50*	1,070	*270*
Sr	517	*3*	510	*10*	546	*4*	511	*5*
Y	944	*32*	965	*95*	834	*8*	1,090	*90*
La	4,030	*90*	3,790	*350*	5,020	*60*	4,180	*300*
Ce	5,040	*130*	5,260	*380*	5,710	*80*	5,720	*350*
Pr	426	*13*	470	*30*	446	*7*	508	*32*
Nd	1,440	*40*	1,590	*90*	1,410	*20*	1,710	*120*
Sm	216	*7*	238	*15*	197	*4*	257	*21*
Eu	17.9	*0.4*	19.3	*0.9*	18.9	*0.2*	20.1	*0.8*
Gd	202	*7*	217	*17*	180	*3*	236	*19*
Tb	25.6	*0.8*	27.2	*2.4*	22.3	*0.3*	29.9	*2.7*
Dy	151	*5*	160	*15*	132	*1*	178	*16*
Ho	29.9	*0.9*	31.4	*3.2*	26.1	*0.3*	34.7	*3.1*
Er	82.5	*2.9*	86.1	*8.9*	72.7	*0.9*	96.3	*8.6*
Tm	10.1	*0.3*	10.3	*1.1*	8.91	*0.1*	11.5	*0.9*
Yb	54.7	*1.7*	55.7	*6.1*	50.9	*0.6*	61.7	*4.6*
Lu	6.22	*0.13*	6.16	*0.64*	6.25	*0.08*	6.61	*0.43*
Th	395	*8*	304	*20*	363	*8*	365	*38*
U	15.6	*0.4*	16.6	*1.2*	14.8	*0.2*	20.6	*1.3*

BLE 3. Phosphorous (in ppm) and REE concentrations (in ppb) in the quenched experimental fluids measured by solution ICP-M

lement	Ap150_1	Ap150_2_REE	Ap150_3_REE	Ap150_4	Ap150_5_REE	Ap150_6_REE	Ap250_1	Ap250_2	Ap250_3
(ppm)	16.6	50.9	62.3	BDL	33.5	24.5	165	184	15.0
(ppb)	BDL	68.3	1.07	BDL	9.82	5.64	149	139	4.37
a	24.7	136	24.8	22.8	39.5	39.1	720	643	0.44
e	23.0	143	20.6	18.2	40.5	35.1	1089	976	BDL
r	1.45	79.2	2.24	1.53	12.6	8.47	99.8	90.0	BDL
d	2.05	88.2	2.74	1.83	15.4	10.3	338	303	BDL
m	2.17	68.0	3.29	2.52	11.7	6.89	52.8	49.3	1.39
u	2.39	66.4	3.44	2.70	11.4	6.89	21.0	21.1	15.0
d	BDL	79.2	BDL	BDL	9.00	4.97	50.5	46.9	15.1
b	24.7	87.1	26.0	25.2	32.2	29.2	14.7	14.6	16.7
y	BDL	66.0	0.57	BDL	9.05	4.32	32.0	31.9	13.0
o	19.6	83.7	20.9	19.8	27.6	24.3	15.4	15.3	7.48
r	4.36	71.1	5.73	4.62	13.6	9.31	22.0	21.5	3.44
m	20.0	83.1	21.4	20.1	27.9	24.7	14.3	14.4	0.10
b	3.75	67.7	5.01	3.72	12.8	8.52	18.6	18.2	BDL
u	21.6	84.0	23.1	21.7	29.6	26.4	12.5	12.6	4.02

***BDL = below detection limit**

TABLE 3 (Continued)

	Ap250_4_REE	Ap250_5_REE	Ap250_6	Ap250_8_REE	Ap250_9_REE	Ap250_10_REE	Ap250_11
P (ppm)	30.7	105	0.55	BDL	18.0	10.0	17.1
Y (ppb)	432	154	15.5	15.5	73.6	89.4	32.7
La	536	207	16.3	17.2	83.9	114	41.5
Ce	579	223	17.7	19.1	313	125	59.7
Pr	482	151	6.81	6.87	80.1	116	51.1
Nd	350	115	3.92	4.45	83.6	117	53.1
Sm	472	147	3.24	3.28	103	144	72.5
Eu	35.9	20.8	16.8	16.6	103	142	70.9
Gd	425	145	7.42	7.38	107	151	75.3
Tb	467	150	10.7	10.6	101	138	70.1
Dy	466	146	4.87	4.85	99.6	135	67.4
Ho	466	139	10.7	10.6	99.0	132	65.3
Er	469	134	8.44	8.35	104	133	68.8
Tm	467	123	12.9	12.7	96.8	121	60.0
Yb	462	114	9.99	9.87	99.6	117	59.0
Lu	467	119	11.5	11.4	75.5	86.8	38.8

BLE 4. $(REE/P)_{fluid}/(REE/P)_{apatite}$ ratios calculated from unreacted starting apatite rims (Table 2) and the composition of the reac
experimental fluids (Table 3).

Experiment	pH	Starting condition	Y	La	Ce	Pr	Nd	Sm	Eu
Ap150_1	3	-	BDL	0.08	0.06	0.04	0.02	BDL	BDL
Ap150_2_REE	3	0.5 wt% NaCl; 1 ppm REE	0.32	0.15	0.11	0.70	0.23	1.31	15.7
Ap150_3_REE	3	5 wt% NaCl; 1 ppm REE	BDL	0.02	0.01	0.02	0.01	0.02	0.28
Ap150_5_REE	4	0.5 wt% NaCl; 1 ppm REE	0.06	0.07	0.05	0.17	0.06	0.30	3.54
Ap150_6_REE	4	5 wt% NaCl; 1 ppm REE	0.06	0.09	0.06	0.16	0.06	0.27	3.26
Ap250_1	2	-	0.20	0.24	0.27	0.27	0.27	0.29	1.40
Ap250_2	2	-	0.17	0.20	0.21	0.22	0.22	0.24	1.25
Ap250_3	3	-	0.06	BDL	BDL	BDL	BDL	0.08	11.0
Ap250_4_REE	3	0.5 wt% NaCl; 1 ppm REE	3.10	0.98	0.76	7.10	1.52	13.8	12.9
Ap250_5_REE	3	5 wt% NaCl; 1 ppm REE	0.32	0.11	0.09	0.65	0.15	1.25	2.17
Ap250_6	4	-	6.18	1.63	1.32	5.73	0.97	4.86	339
Ap250_8_REE	4	1 ppm REE	0.90	0.26	0.70	2.01	0.62	5.12	63.0
Ap250_9_REE	4	0.5 wt% NaCl; 1 ppm REE	1.97	0.64	0.51	5.25	1.57	12.9	156
Ap250_10_REE	4	5 wt% NaCl; 1 ppm REE	0.42	0.13	0.14	1.35	0.41	3.81	45.7
Ap250_11	4	-	0.34	0.03	BDL	0.09	BDL	0.75	49.2

***BDL = below detection limit**

TABLE 4. continued

Gd	Tb	Dy	Ho	Er	Tm	Yb	Lu
BDL	10.8	BDL	7.23	0.33	22.3	0.37	40.8
1.52	14.3	1.90	12.0	3.77	36.2	5.56	61.1
0.00	3.06	BDL	2.09	0.15	6.50	0.19	11.9
0.26	7.40	0.34	5.48	0.96	16.9	1.39	30.0
0.20	9.46	0.26	6.81	0.97	21.1	1.38	37.7
0.30	0.71	0.26	0.61	0.33	1.74	0.44	2.71
0.25	0.63	0.23	0.55	0.29	1.56	0.37	2.43
0.99	8.72	1.16	3.39	0.56	0.14	BDL	9.23
13.5	119	20.2	103	37.8	314	57.5	525
1.35	11.1	1.84	8.91	3.14	24.0	4.13	39.0
12.4	156	12.1	135	35.8	485	69.2	750
5.82	43.8	7.40	37.2	14.3	111	21.2	144
14.8	108	18.0	89.4	32.9	250	44.7	301
4.29	32.0	5.21	25.7	9.96	72.3	13.2	78.7
4.70	41.5	5.56	16.95	3.24	6.77	BDL	50.4

FIGURE 1. Cathodoluminescence images of unreacted starting apatite showing growth zonings. (**a**) Section perpendicular to c-axis, (Durango A in Table 2). (**b**) Section parallel to c-axis (Durango B in Table 2). Also given are the locations of LA-ICP-MS analytical spots. Spot numbers for transects correspond to those given in Figures 2 and 3. Elemental concentration data are shown in Figures 2 and 3. Note that (**b**) only shows a portion of the transect.

FIGURE 2. Element concentrations obtained by LA-ICP-MS of unreacted apatite along a transect perpendicular to the c-axis. The locations of the analytical spots are given in Fig. 1a.

FIGURE 3. Element concentrations obtained by LA-ICP-MS of unreacted apatite along a transect parallel to the c-axis. The locations of the analytical spots are given in Fig. 1b.

FIGURE 4. Backscattered electron images of apatite reacted with a fluid containing HCl (a, c) and $HClO_4$ (b, d) at 150 and 250 °C for ~9 days. The experiment in b) was also doped with 1 ppm REE. The images show an increase in the formation of etch pits and the precipitations of secondary monazite-(Ce) with increased temperatures and decreased pH. Experimental starting conditions and secondary REE phosphate minerals identified are listed in Table 1.

FIGURE 5. Backscattered electron images of apatite reacted at pH of 3 to 4 at 150 °C (a, b) and 250 °C (c, d) with HCl-bearing fluids containing 0.5 wt% NaCl and doped with 1 ppm REE. The reacted crystals display a preferred formation of etch pits and dissolution channels along the c-axis and precipitations of secondary monazite-(Ce).

FIGURE 6. Backscattered electron images of apatite reacted at pH of 3 to 4 at 150 °C (a, b) and 250 °C (c, d) with HCl-bearing fluids containing 5 wt% NaCl and doped with 1 ppm REE. The reacted crystals display a preferred formation of etch pits which follow the c-axis.

FIGURE 7. Backscattered electron images of apatite (crystals from Fig. 6a, b, and d) reacted at pH of 3 to 4 with HCl-bearing fluids containing 5 wt% NaCl and doped with 1 ppm REE. Intergrowths of secondary monazite-(Ce) and REE-rich apatite occur in the etch pits. Corresponding SEM-EDS spectra show diagnostic REE peaks of monazite-(Ce) and Ca peaks for secondary apatite.

FIGURE 8. Concentrations of P and REE (ppb; solution ICP-MS) in the reacted aqueous fluids plotted as a function of starting salinity of the experiments. Experiments were conducted at 150 and 250 °C and pH of 2 to 4. Experiments with 0.5 to 5 wt% NaCl were initially doped with 1 ppm REE. (**a**) Phosphorous concentrations provide a measure of the amount of dissolved apatite. (**b, c**) Light REE and (**d, f**) heavy REE concentrations indicate how much REE was released from the apatite during dissolution and not incorporated into secondary REE phosphates.

FIGURE 9. Mass balance calculations showing the molar REE/P ratios between dissolved elements in the reacted aqueous fluid and ratios in the apatite crystal. Data plotting on the stoichiometric line corresponds to predicted REE and P concentrations from stoichiometric apatite dissolution, data above the line indicate potential precipitation of secondary apatite, and

data below the line indicate potential monazite-(Ce) precipitation. Experimental conditions and calculated ratios are listed in Table 4.

FIGURE 10. Mass balance calculations showing the molar REE/P ratios between dissolved elements in the reacted saline aqueous fluid initially doped with 1 ppm REE and ratios in the apatite crystal. Data plotting on the stoichiometric line corresponds to predicted REE and P concentrations from stoichiometric apatite dissolution, data above the line indicate increased REE mobility, and data below the line indicate potential monazite-(Ce) precipitation. Experimental conditions and calculated ratios are listed in Table 4.

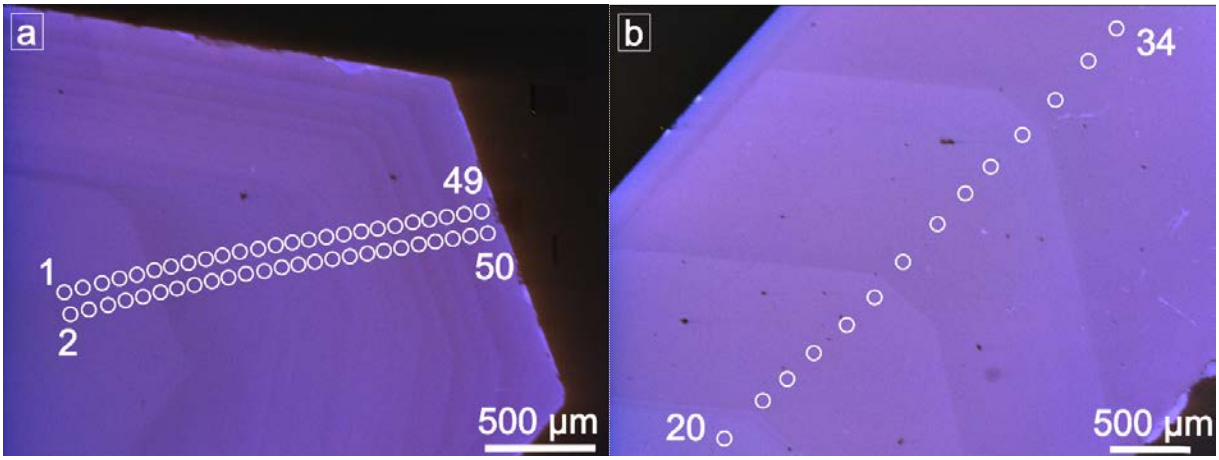

FIGURE 1.

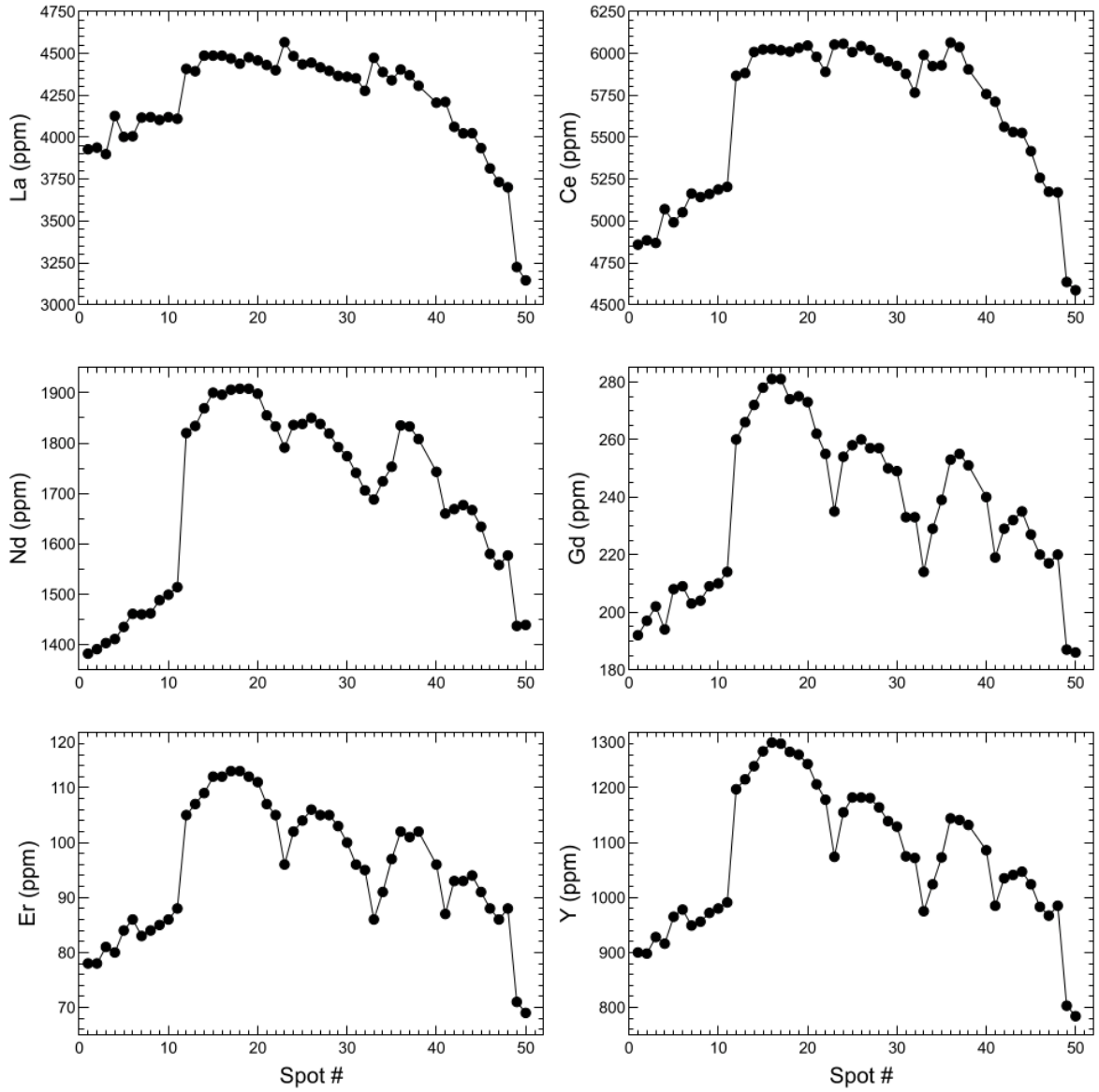

FIGURE 2.

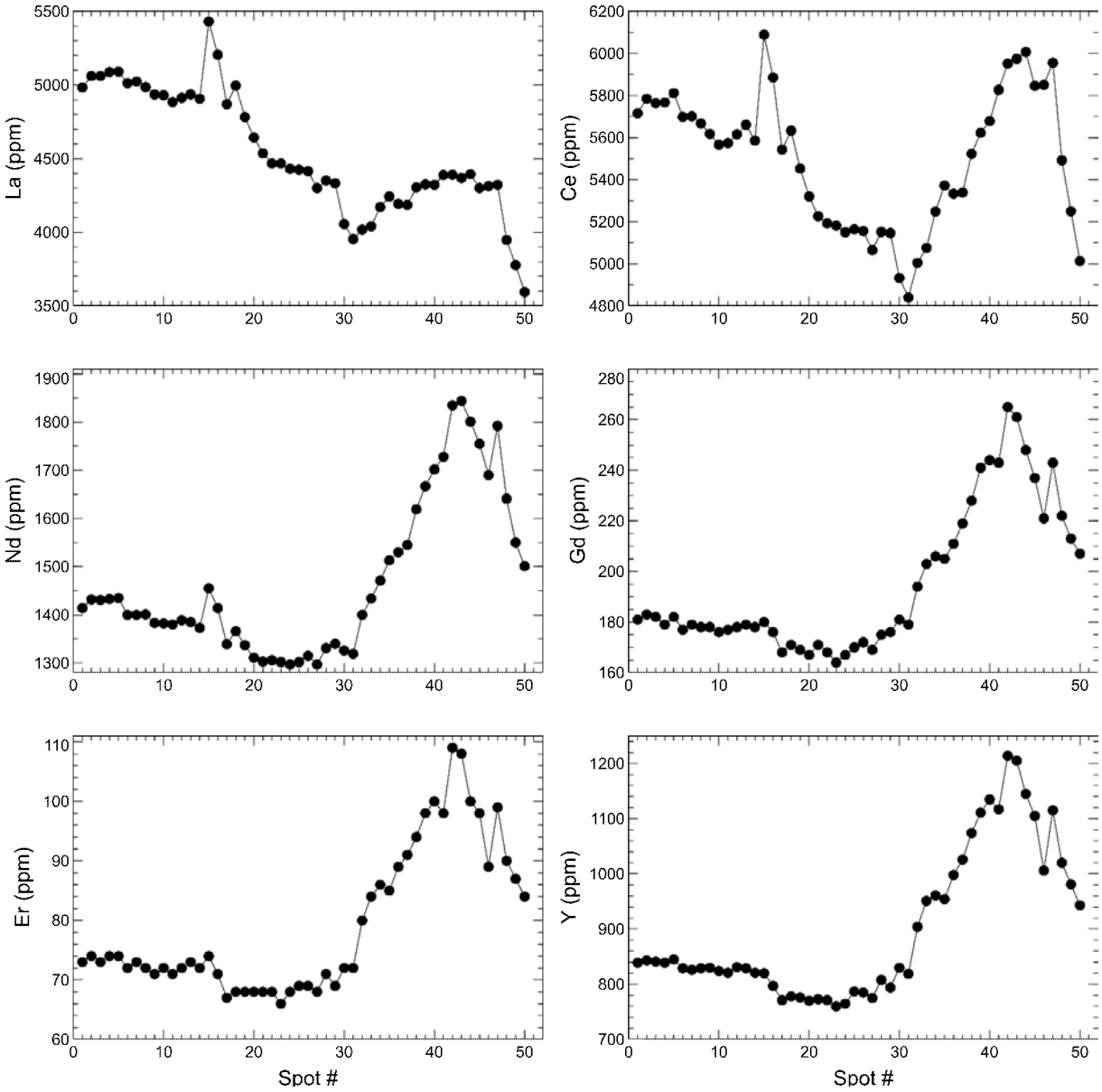

FIGURE 3.

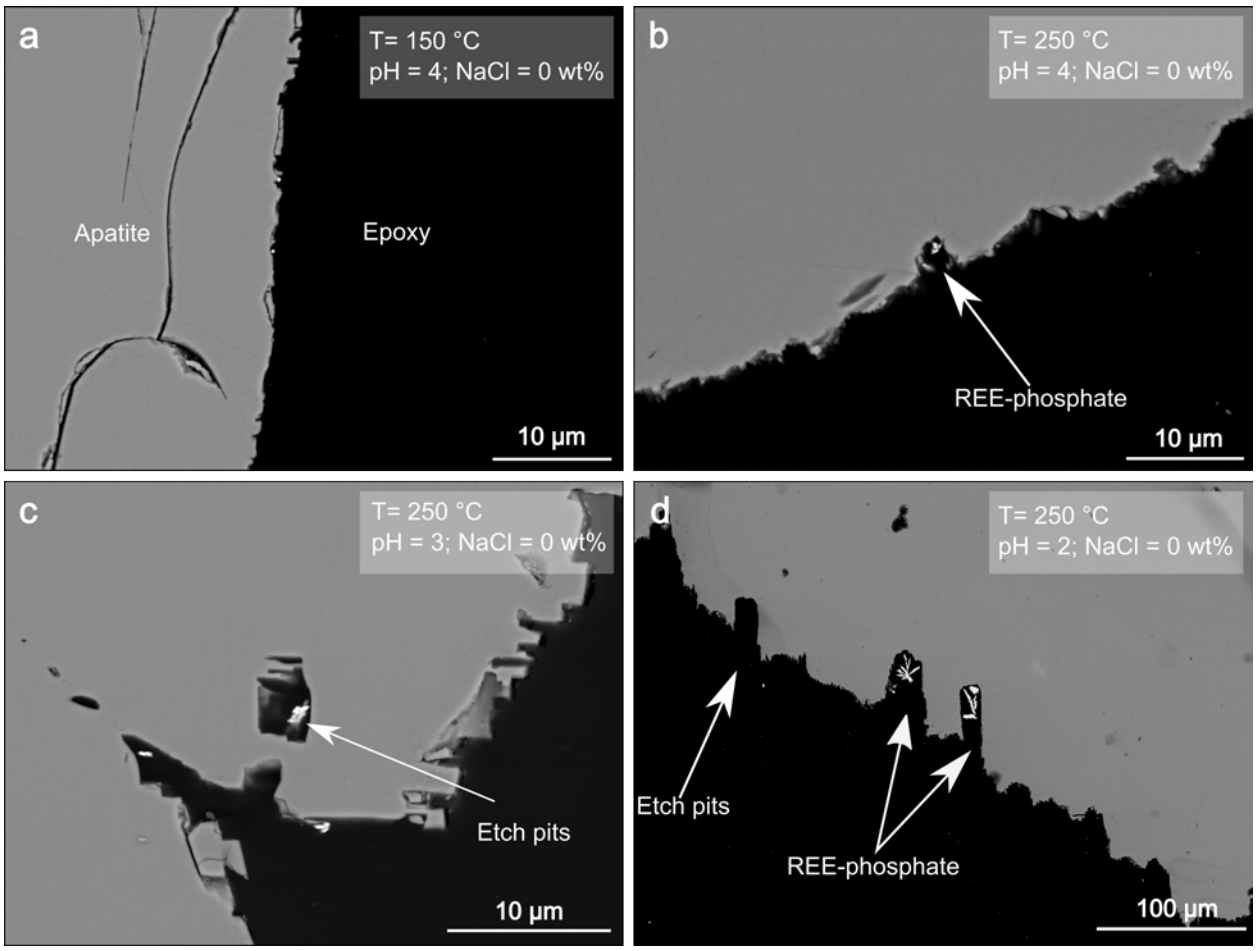
a
T= 150 °C
pH = 4; NaCl = 0 wt%
Apatite
Epoxy
10 µm
b
T= 250 °C
pH = 4; NaCl = 0 wt%
REE-phosphate
10 µm
c
T= 250 °C
pH = 3; NaCl = 0 wt%
Etch pits
10 µm
d
T= 250 °C
pH = 2; NaCl = 0 wt%
Etch pits
REE-phosphate
100 µm

FIGURE 4.

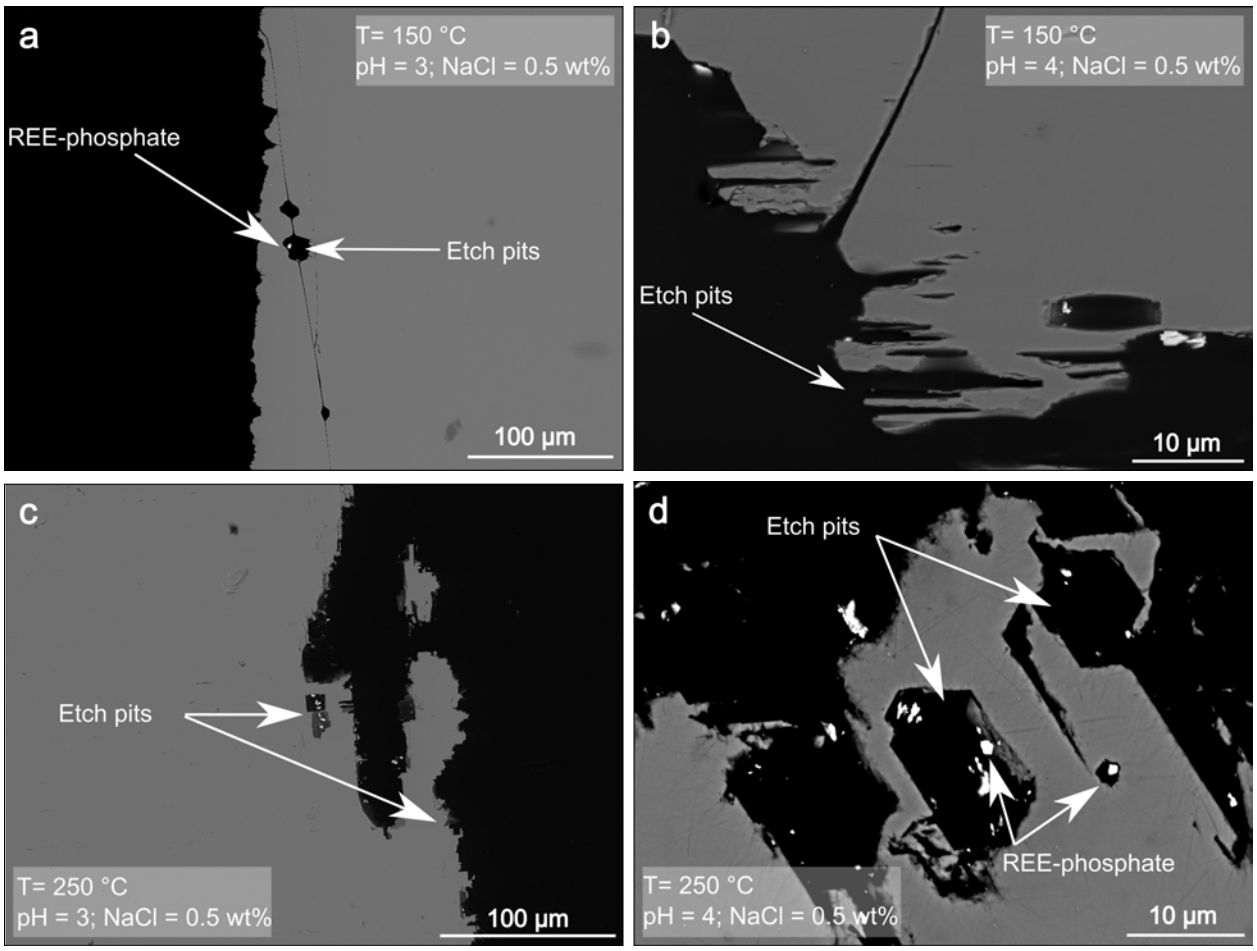
a
T= 150 °C
pH = 3; NaCl = 0.5 wt%
REE-phosphate
Etch pits
100 µm
b
T= 150 °C
pH = 4; NaCl = 0.5 wt%
Etch pits
10 µm
c
Etch pits
T= 250 °C
pH = 3; NaCl = 0.5 wt%
100 µm
d
Etch pits
REE-phosphate
T= 250 °C
pH = 4; NaCl = 0.5 wt%
10 µm

FIGURE 5.

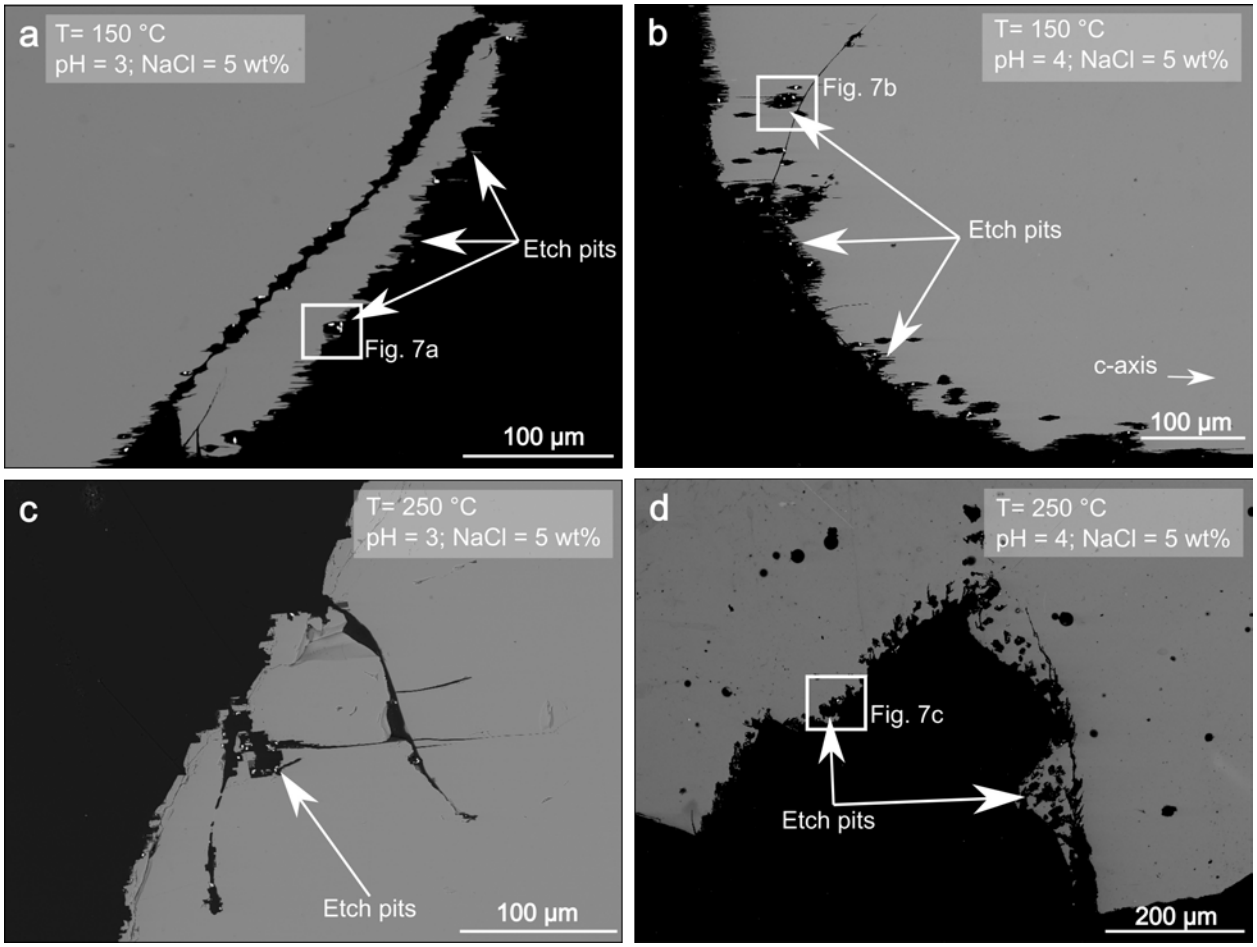
a
T= 150 °C
pH = 3; NaCl = 5 wt%
Etch pits
Fig. 7a
100 µm
b
T= 150 °C
pH = 4; NaCl = 5 wt%
Fig. 7b
Etch pits
c-axis
100 µm
c
T= 250 °C
pH = 3; NaCl = 5 wt%
Etch pits
100 µm
d
T= 250 °C
pH = 4; NaCl = 5 wt%
Fig. 7c
Etch pits
200 µm

FIGURE 6.

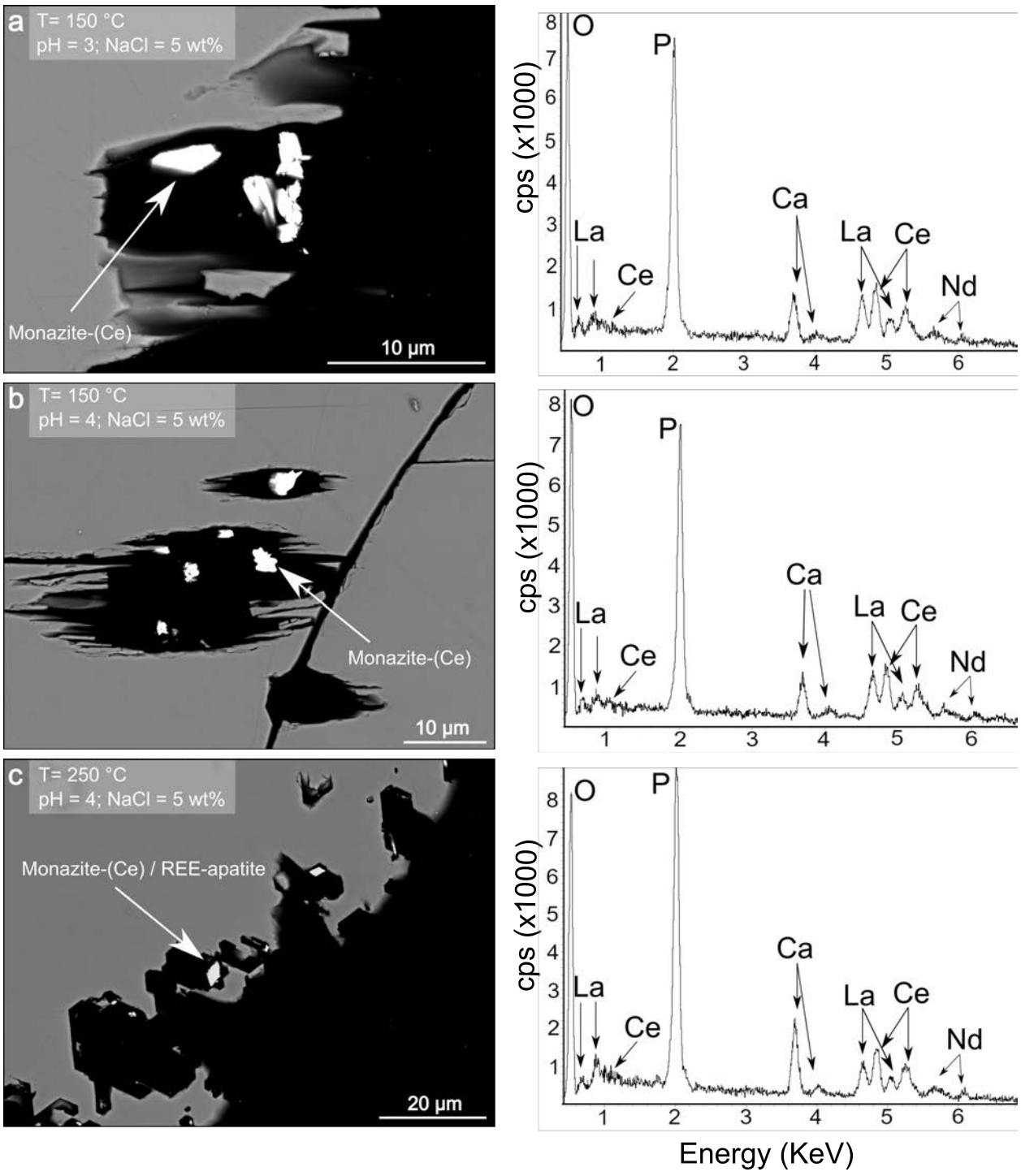
a
T= 150 °C
pH = 3; NaCl = 5 wt%
Monazite-(Ce)
10 µm
b
T= 150 °C
pH = 4; NaCl = 5 wt%
Monazite-(Ce)
10 µm
c
T= 250 °C
pH = 4; NaCl = 5 wt%
Monazite-(Ce) / REE-apatite
20 µm
cps (x1000)
O
P
Ca
La
Ce
Nd
Energy (KeV)

FIGURE 7.

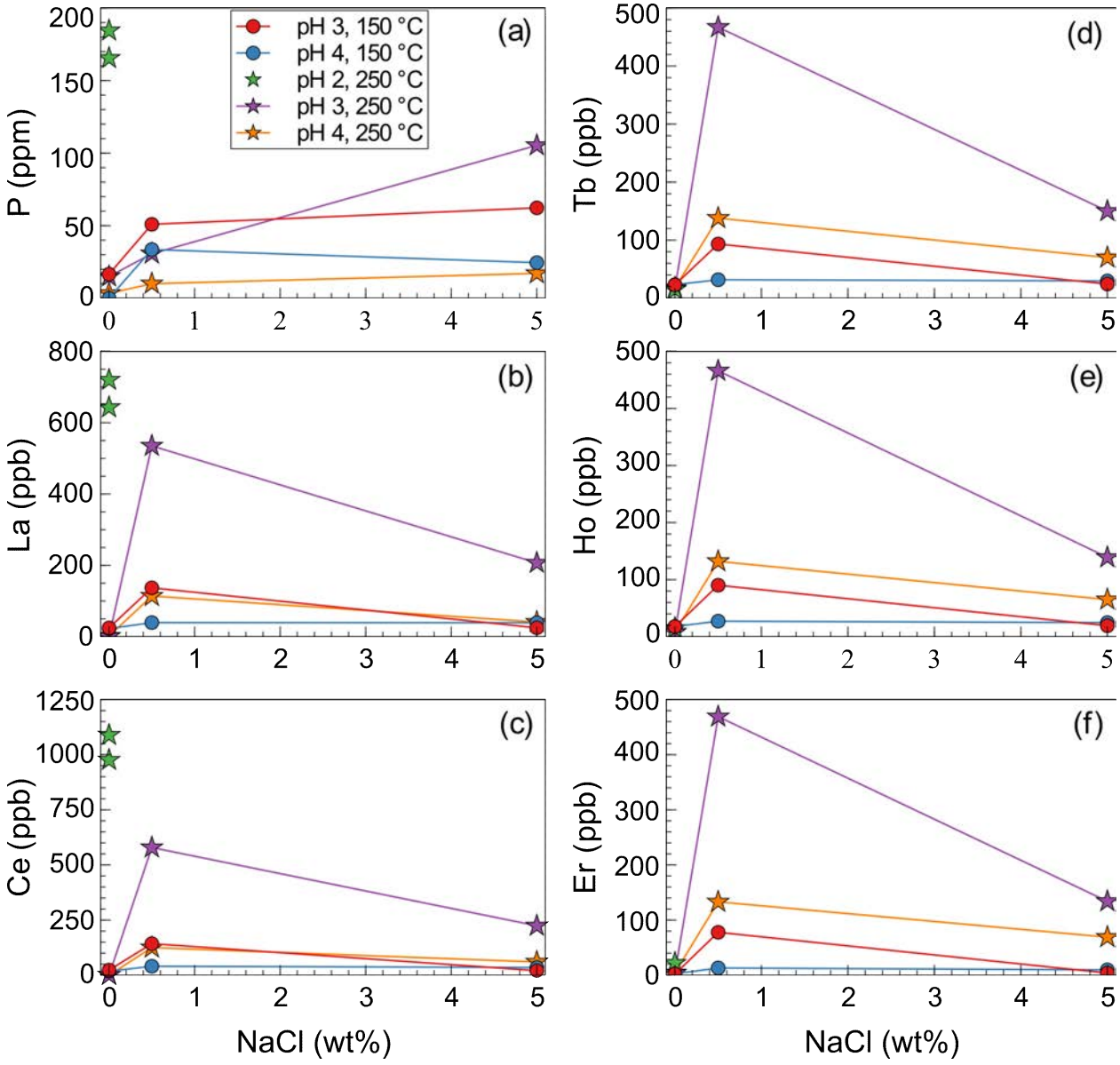
pH 3, 150 °C
pH 4, 150 °C
pH 2, 250 °C
pH 3, 250 °C
pH 4, 250 °C
(a)
P (ppm)
(b)
La (ppb)
(c)
Ce (ppb)
(d)
Tb (ppb)
(e)
Ho (ppb)
(f)
Er (ppb)
NaCl (wt%)
NaCl (wt%)

FIGURE 8.

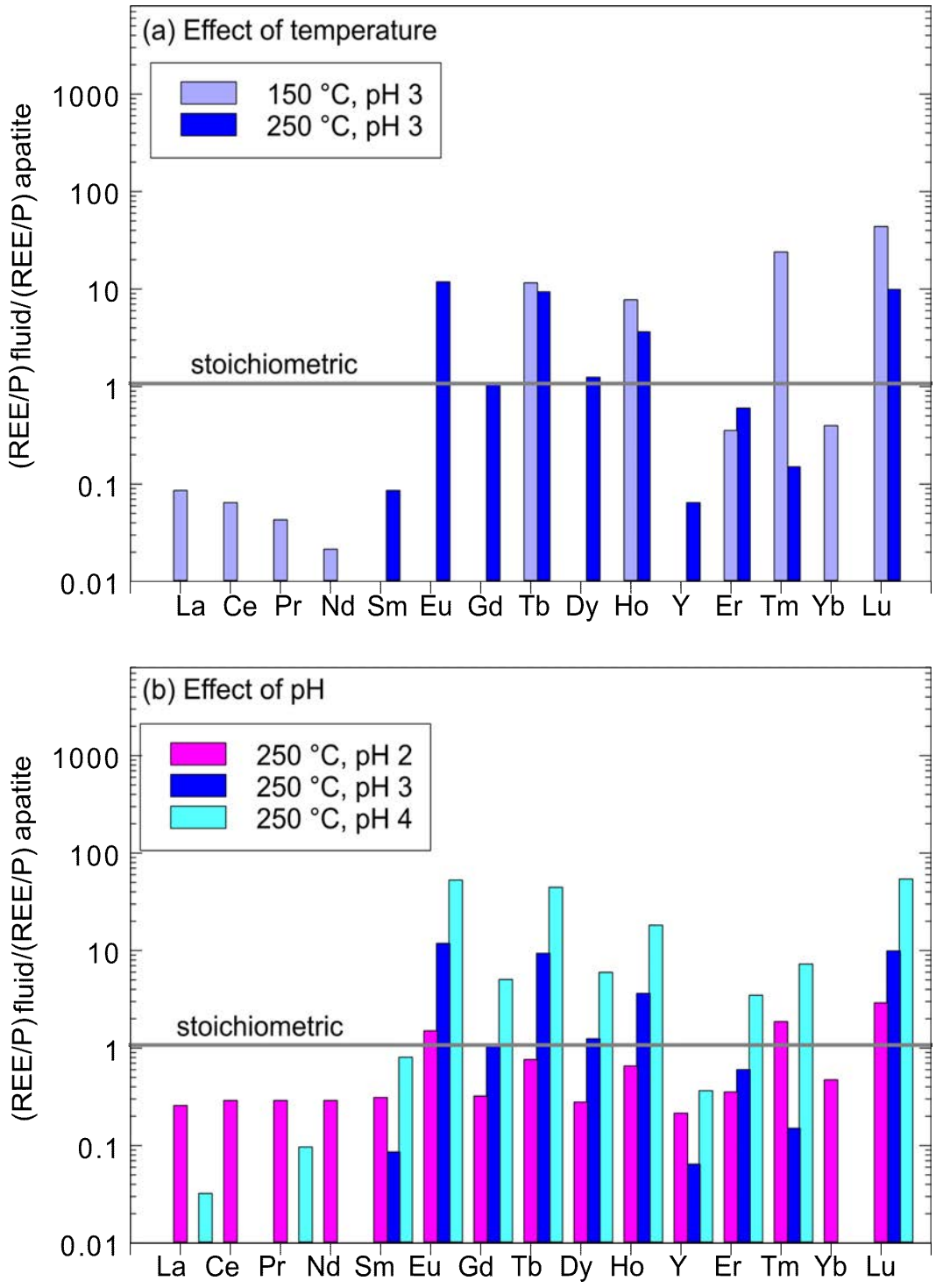
(a) Effect of temperature
150 °C, pH 3
250 °C, pH 3
stoichiometric
(REE/P) fluid/(REE/P) apatite
1000
100
10
1
0.1
0.01
La Ce Pr Nd Sm Eu Gd Tb Dy Ho Y Er Tm Yb Lu
(b) Effect of pH
250 °C, pH 2
250 °C, pH 3
250 °C, pH 4
stoichiometric
(REE/P) fluid/(REE/P) apatite
1000
100
10
1
0.1
0.01
La Ce Pr Nd Sm Eu Gd Tb Dy Ho Y Er Tm Yb Lu

FIGURE 9.

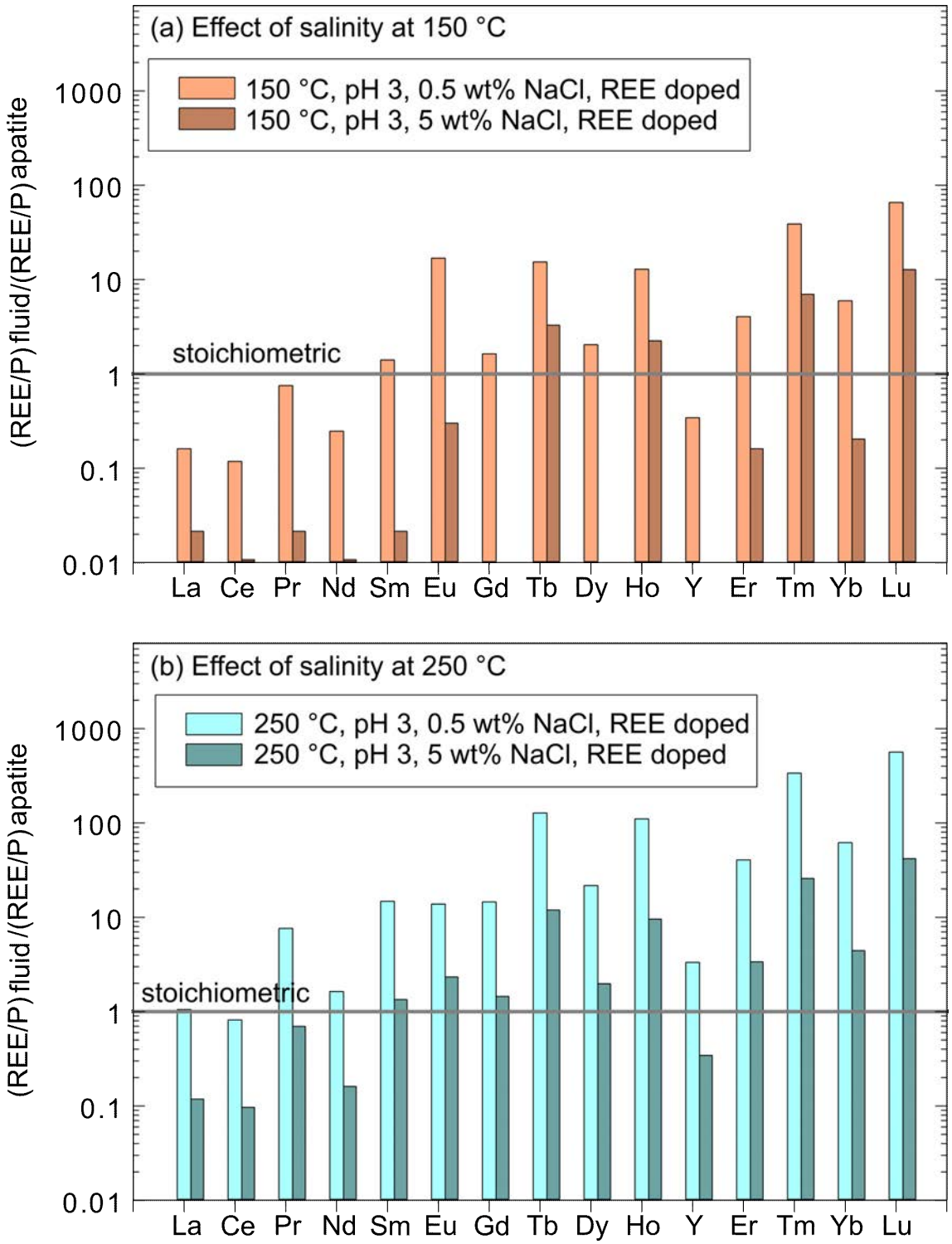
(a) Effect of salinity at 150 °C
150 °C, pH 3, 0.5 wt% NaCl, REE doped
150 °C, pH 3, 5 wt% NaCl, REE doped
(REE/P)fluid/(REE/P)apatite
1000
100
10
1
0.1
0.01
stoichiometric
La Ce Pr Nd Sm Eu Gd Tb Dy Ho Y Er Tm Yb Lu
(b) Effect of salinity at 250 °C
250 °C, pH 3, 0.5 wt% NaCl, REE doped
250 °C, pH 3, 5 wt% NaCl, REE doped
(REE/P)fluid/(REE/P)apatite
1000
100
10
1
0.1
0.01
stoichiometric
La Ce Pr Nd Sm Eu Gd Tb Dy Ho Y Er Tm Yb Lu

FIGURE 10.